Occupational exposure during handling and loading of halloysite nanotubes – A case study of counting nanofibers

Koivisto, Antti Joonas; Bluhme, Anders Broström; Kling, Kirsten Inga; Fonseca, Ana Sofia; Redant, Emile; Andrade, Flavia; Hougaard, Karin Sørig; Krepker, Maksym; Prinz, Ofer Setter; Segal, Ester; Holländer, Andreas; Jensen, Keld Alstrup; Vogel, Ulla ; Koponen, Ismo Kalevi

Published in:
NanoImpact

Link to article, DOI:
10.1016/j.impact.2018.04.003

Publication date:
2018

Document Version
Publisher's PDF, also known as Version of record

NanoImpact 10 (2018) 153–160

Contents lists available at ScienceDirect

NanoImpact

journal homepage: www.elsevier.com/locate/nanoimpact

Research paper

Occupational exposure during handling and loading of halloysite nanotubes – A case study of counting nanofibers

Antti Joonas Koivisto[a,*], Anders Brostrøm Bluhme[a,b], Kirsten Inga Kling[a], Ana Sofia Fonseca[a], Emile Redant[c], Flavia Andrade[c], Karin Sørig Hougaard[a], Maksym Krepker[d], Ofer Setter Prinz[d], Ester Segal[d], Andreas Holländer[e], Keld Alstrup Jensen[a], Ulla Vogel[a], Ismo Kalevi Koponen[a]

[a] National Research Centre for the Working Environment, Lersø Parkallé 105, Copenhagen DK-2100, Denmark
[b] Technical University of Denmark, Department of Micro- and Nanotechnology, Ørsteds Plads, Building 345B, DK-2800 Kgs. Lyngby, Denmark
[c] Bio Base Europe Pilot Plant, Rodenhuizekaai 1, 9024 Gent, Belgium
[d] Department of Biotechnology and Food Engineering, Technion - Israel Institute of Technology, Haifa 32000, Israel
[e] Fraunhofer Allianz POLO, Fraunhofer-Institut für Angewandte Polymerforschung, Geiselbergstr. 69, 14476 Potsdam, Germany

ARTICLE INFO

Keywords:
Halloysite nanotubes
Inhalation exposure
High aspect ratio nanomaterial (HARN)
Nanofiber counting
Occupational exposure limit

ABSTRACT

Halloysite nanotubes (HNTs) are abundant naturally-occurring hollow aluminosilicate clay mineral fibers with a typical diameter < 100 nm and an aspect ratio of up to 200. Here we assessed the potential inhalation exposure to HNTs in an industrial research laboratory. Inside a fume hood, ten times 100 g of HNTs were poured at rate of 0.5 kg min^{-1}, which increased concentrations from the background level up to 2900 cm^{-3} and 6.4 μm^2 cm^{-3}. Inside the fume hood, the respirable mass concentration was 143 μg m^{-3} including background particles. Outside the fume hood we did not measure elevated concentrations. We classified 1895 particles according to their length and aspect ratio. Five particles were in aspect ratio > 3 and in length > 2 μm. These particles were agglomerated and/or aggregated particles where the longest individual fiber was 2 μm in length. The occupational exposure limits for refractory mineral fibers vary from 0.1 to 2 fibers cm^{-3}. Following standard protocols for fiber analysis, detection of 0.1 fibers cm^{-3} would require analysis on 4 × 10^4 images when the filter loading is good. Thus, the fiber sampling and quantification procedures needs to be improved significantly if nanofibers < 100 nm in diameter are included in regulatory exposure assessment. Due to very limited toxicological information of HNTs we recommend avoiding inhalation exposure.

1. Introduction

Halloysite nanotubes (HNTs) are a low cost and naturally occurring abundant clay mineral of the kaolin group (Joussein et al., 2005). HNTs are hollow insoluble mineral fibers with lengths of up to 30 μm and aspect ratio values of up to 200 (Makaremi et al., 2017). They are characterized by high mechanical strength and modulus, and due to their hollow nanostructure they are widely used for loading and controlled release of functional compounds (Makaremi et al., 2017; Yang et al., 2016; Huang et al., 2016; Saif and Asif, 2015; Lvov et al., 2016a). HNTs are used in, *e.g.*, self-healing anticorrosive coatings (Wei et al., 2015), hydrogen production and storage (Sahiner and Sengel, 2017; Jin et al., 2017), pharmaceutical excipients (Hanif et al., 2016; Lvov et al., 2016b; Yendluri et al., 2017), biomedical applications (Liu et al., 2016; Bonifacio et al., 2017), cosmetics (Saif and Asif, 2015), active food packaging materials (Shemesh et al., 2016; Tas et al., 2017; Krepker et al., 2017), water treatment (Yu et al., 2016), and for improvement the mechanical properties and thermal stability of polymer composites (Liu et al., 2014). Globally, HNTs annual production is over 50,000 metric tonnes (Lvov et al., 2008), which is similar to that of carbon fibers (40,000 t/y; Gutiérrez and Bono, 2013), and approximately 10 times higher than the production of carbon nanotubes which is only *ca.* 4000 t/y (De Volder et al., 2013).

Pulmonary exposure to long and poorly soluble fibers is associated with a high risk of serious adverse health effects (*e.g.* Lippmann, 1988). It has been shown that mesothelioma and pleural plaques are caused by biodurable fibers thinner than ~0.1 μm and longer than ~5 μm while cancer and pulmonary fibrosis are caused by fibers thicker than ~0.1 μm and longer than ~20 μm (Lippmann, 1988). This phenomenon of inhalable, long and biodurable fibers is denoted the fiber paradigm, and fibers fulfilling the criteria are defined as WHO fibers (Lippmann, 1988, 2014; Harrison et al., 2015). Another important hazard indicator

* Corresponding author.
E-mail address: jok@nrcwe.dk (A.J. Koivisto).

https://doi.org/10.1016/j.impact.2018.04.003
Received 27 February 2018; Received in revised form 9 April 2018; Accepted 11 April 2018
Available online 12 April 2018

for HNTs is their high aspect ratio and large specific surface area. For mineral fibers with a diameter in the range of 0.15 and 2 μm and a length above 2 μm, fibrosis correlated with the surface area of the fibers (Lippmann, 1988, 2014; Stayner et al., 2008, 2013; Hwang et al., 2014). While airway exposure to short carbon nanotubes, ~0.3 μm in length, was shown to cause fibrosis and long lasting inflammation (Pauluhn, 2010; Poulsen et al., 2015, 2016, 2017).

The occupational exposure limits (OELs) for refractory mineral fibers fulfilling the fiber paradigm generally vary from 0.1 to 2 fibers cm^{-3} (Harrison et al., 2015; Nielsen and Koponen, 2018). For high aspect ratio nanomaterials (HARN), such as non-entangled carbon nanotubes, carbon nanofibres, and nanocellulose, with fiber lengths over *ca.* 5 μm, a more stringent OEL of 0.01 fibers cm^{-3} has been proposed for precautionary reasons (Mihalache et al., 2017). Gebel et al. (2014) proposed that biodurable HARN that do not meet the fiber paradigm may be classified as granular biodurable particles (GBPs). GBPs are classified as low toxicity particles, which may however cause inflammation and acute phase response (Moreno-Horn and Gebel, 2014; Saber et al., 2014), which in turn are risk factors for cardiovascular disease (Saber et al., 2014).

Stanton et al. (1981) showed that pleural dose to 40 mg of two different types of HNTs in hardened gelatin implanted on to the pleural surface resulted in formation of pleural sarcomas in 9 of 53 rats (17%) 2 years post-exposure as compared to 3 of 488 sham-treated controls (0.6%). Kaolin, a platy sheet silicate with similar chemical composition as HNTs, has been shown to induce cytotoxicity and genotoxicity in isolated rat alveolar macrophages (Gao et al., 2000). Unmodified HNTs have shown to induce very low cytotoxicity in the following human cell types: carcinoma cells, peripheral blood lymphocytes, primary umbilical vein endothelial cells, intestinal cells, and epithelial cells (Ahmed et al., 2015; Vergaro et al., 2010; Nan et al., 2008; Lai et al., 2013). However, as HNTs have similar dimensions as short carbon nanotubes (CNTs), they may potentially cause pulmonary inflammation and acute phase response following pulmonary exposure as previously reported for CNTs (Saber et al., 2013, 2014; Poulsen et al., 2015, 2017; Jaurand, 2017).

Here, we studied HNTs release and exposure during a two-step loading process where HNTs are mixed with essential oil. The product is used for example in active food packaging materials, which have been reported to reduce bacterial growth by up to seven orders of magnitude, thereby increasing the shelf life of perishable foods (Shemesh et al., 2016; Tas et al., 2017; Krepker et al., 2017). Here we assessed workers inhalation exposure by measuring air concentrations using diffusion chargers and by sampling airborne particles for gravimetric and electron microscopy analysis. Subsequent risk assessment was performed based on HNTs exposure levels in fiber number, surface area, and mass concentrations. Finally, we discuss the potential challenges in fiber counting when the fiber diameter is < 100 nm.

2. Experimental section

2.1. Measurement strategy

Particle concentrations were measured from different locations named here as fume hood (30 cm above the mixing bowl), near-field at a height of 1.5 m, breathing zone, and incoming ventilation air using four miniature diffusion size classifiers (DiSCmini, Matter Aerosol AG, Wohlen, Switzerland) and four respirable particle samplers (Fig. 1). The DiSCminis were equipped with 0.7 μm pre-separators and *ca.* 50 cm Tygon sampling hoses. The DiSCminis readings were compared before the measurements started by sampling room air aerosol for 240 s within with 10 cm radius. The DiSCminis showed good agreement between all four instruments when measuring at the same location (Fig. 2) as has also been observed in previous studies (Bau et al., 2017). The correlations as compared to average values measured by the DiSCminis were for *N* from 0.63 to 0.87, *LSDA* from 0.69 to 0.90 and $D_{p,DM}$ from 0.60 to 0.77 (Table S6, Supporting Information).

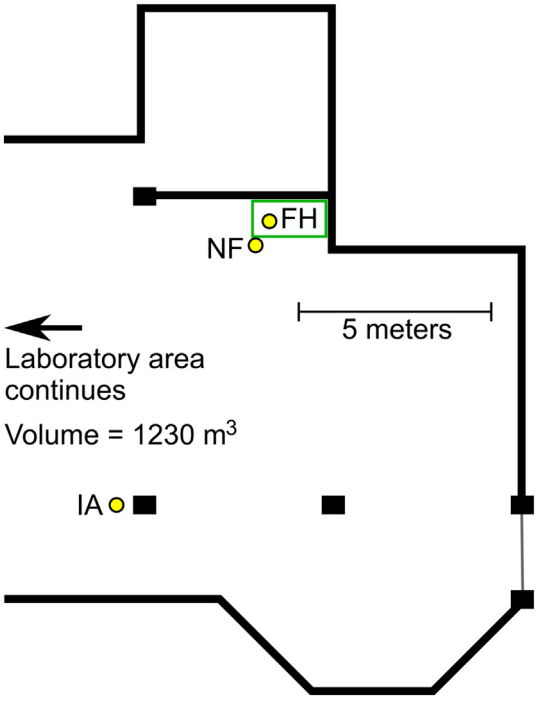

Fig. 1. Layout of the laboratory and sampling locations of Incoming Air of mechanical ventilation air inlet (IA), Near-Field (NF), and Fume Hood (FH).

Respirable particles were collected on a pre-weighted 37 mm Teflon filters with a 0.8 μm pore size (Millipore, Billerica, MA, USA) using a BGI Model GK2.69 (Q_s = 4.2 L min^{-1}) Triplex cyclones (BGI Inc., Waltham, MA, USA; Stacey et al., 2014). Three control blind filters were used to correct for handling and environmental factors. Filter weighing was completed in a climate controlled weighing room at 50% relative humidity and 22 °C after at least 24-hour acclimatization. The fume hood air flow was measured using a hot wire anemometer (BL-30 AN, Voltcraft, Hirschau, Germany).

2.2. Particle sampling and characterization

The sample was collected at a flow rate of 0.5 L min^{-1} (model NMP 830, KNF Neuberger, Germany) using a Micro Inertial Impactor (Kandler et al., 2007), consisting of three stages, each equipped with Nickel TEM grids with a Formvar carbon foil. This sampling technique has been used successfully in environmental (Lieke et al., 2011; Kandler et al., 2011; Nguyen et al., 2017), occupational (Jensen et al., 2015; Kling et al., 2016; Koivisto et al., 2018), and combustion particle studies (Lieke et al., 2013). The Micro Inertial Impactor samples particles up to *ca.* 30 μm in diameter depending on the sample flow's iso-axial behavior (Kandler et al., 2007). The calculated d_{50} cut-off diameters by inertial impaction are 1.3, 0.5, and 0.05 μm for the impaction stages. The particle collection size ranges by inertial impaction are:

- Stage 1: 1.3 μm < d_p < ~30 μm
- Stage 2: 0.5 μm < d_p < 1.3 μm
- Stage 3: 0.05 μm < d_p < 0.5 μm

Here we took overview images of the samples from each stage which was used to locate the impaction spots which were analyzed in further detail at higher magnifications, sufficiently high for resolving the nano-scale dimensions suspected in the sample.

The analysis was made at the Center for Electron Nanoscopy, Technical University of Denmark, using a FEI Nova NANO Scanning Electron Microscope 600, which was used in scanning transmission

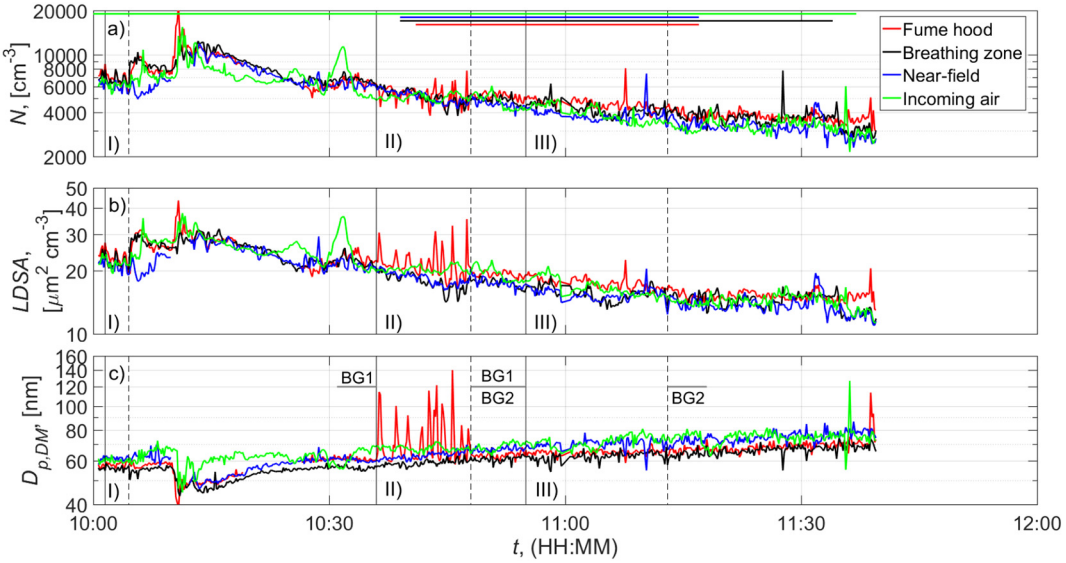

Fig. 2. Particle a) *N* and b) *LDSA* concentrations and c) average particle diameter during pouring of Dragonite HP™ and Carvacrol into a mixing pot and during mixing. Averaging time was 10 s. Thick horizontal lines show the PM_4 collection times and solid and dashed vertical lines show respectively start and end times of the I) DiSCmini instrument comparison, II) Pouring process, and III) Mixing process. Figure c) grey lines shows background concentration averaging times BG1 and BG2. Horizontal lines shows the respirable particle collector sampling periods.

electron microscopy mode to enhance the contrast between substrate and particles. The microscope was operating at an acceleration voltage of 15 kV, and at high vacuum. Images were acquired mainly at magnifications of 15 k, resulting in resolutions of approximately 6 nm pixel^{-1}. A few images were also acquired at higher magnifications of up to 40 k, corresponding to resolutions of 2 nm pixel^{-1} (not shown).

Images were post-processed using python version 2.7 and the open source Computer Vision package (OpenCV v. 3.1; Bradski, 2000). Particles were recognized when their intensities were lower than a specified threshold, and their area larger than a preset minimum. The minimum area was set to 10 pixels (diameter of approximately 3 pixels), since this was found to be the limit for recognizing particles based on the signal to noise ratio of the images. All the images had similar contrast and brightness, which made it possible to segment the images using a simple global threshold value of 120, meaning that pixels with intensities below 120 were marked as particles. The image analysis did not correct for cases with particle co-depositions, as well as agglomerates and aggregates, since only simple thresholding and contour recognition were used before sizing. The area, equivalent diameter (calculated from the area), and aspect ratio were determined for each recognized particle, where aspect ratio was defined as the ratio between the longest, $D_{BB,L}$, and shortest, $D_{BB,s}$, sides of a bounding box (including rotation).

2.3. Fiber counting

The sample air fiber concentration C_f (m^{-3}) is

$$C_f = f \times \frac{A_C}{V} = \frac{N_f}{n_{gf} \times A_{gf}} \frac{A_C}{V}, \quad (1)$$

where f (fibers m^{-2}) is the fiber surface density, A_C (m^2) is the effective collection area of the filter, V (m^3) is the sample volume, N_f (−) is number of counted fibers, n_{gf} (−) is the number of analyzed graticule fields, A_{gf} (m^2) is the graticule field area. The number of graticule fields needed to find a fiber ($N_f = 1$) is

$$n_{gf} = \frac{1}{f \times A_{gf}} \propto \frac{1}{f \times d_{gf}^2}, \quad (2)$$

where d_{gf} (m) is the diameter of the graticule field area. NIOSH estimated inter-laboratory precision for asbestos fibers counted using a phase-contrast microscope counted from 100 graticule fields (NIOSH, 1994a). This should be applicable to the fiber counting from images taken by using electron microscope (NIOSH, 1994b). NIOSH defined the limit of detection as the inter-laboratory variability upper 95% confidence limit on a measured value is 300% grater (4 times) than the measured value (Ashley and O'Connor, 2016; NIOSH, 1994a). This requires counting of at least 5.5 fibers (NIOSH, 1994a).

2.4. Alveolar lung deposited surface area (LDSA) and pulmonary inflammation

Assuming that the HNTs and GBPs induce lung influx of PMN to at a similar degree, the HNT exposure potency to induce pulmonary inflammation can be estimated by comparing the deposited surface area dose with the $NOEL_{1/100}$ of 0.11 cm^2 g^{-1} for GBPs (Koivisto et al., 2016). The $NOEL_{1/100}$ was based on the relationship between polymorphonuclear neutrophilia (PMN) influx in the lungs of rats and mice after a single intratracheal instillation of GBPs and the particles dry powder Brunner-Emmett-Teller (BET) surface area dose normalized with lung weight (cm^2 g^{-1}; Schmid and Stoeger, 2016). The deposited alveolar surface area dose can be calculated by multiplying the LDSA concentration with the inhaled volume. The inhaled volume was estimated for a 70-kg male having a respiratory minute volume of 25 L min^{-1} (ECHA, 2016). During 8-h exposure this corresponds to an inhaled volume of 12 m^3. The deposited alveolar dose was normalized using 840 g the weight of the lungs from a 70-kg male (Molina and DiMaio, 2012). The uncertainties of this risk assessment technique are discussed in detail by Koivisto et al. (2016).

2.5. Work environment and pouring and mixing processes

In the present study, Dragonite HP™ was mixed at a weight ratio 1:1 with carvacrol ($C_{10}H_{14}O$; product code 101839118, Sigma-Aldrich, Steinheim, Germany; CAS: 499-75-2). Both the pouring and the subsequent mixing were performed in a fume hood (POTTEAU, 180 W × 120 H × 70 D, V = 1.5 m^3) located at an industrial research laboratory (Fig. 1). Air velocity at the fume hood opening was 0.43 m s^{-1} at an opening height of 10 cm, the smallest opening possible (opening area 1800 cm^2). The laboratory (room height 2.64 m) was ventilated by natural air exchange and local exhaust ventilations. The replacement

air was outdoor air entering *via* open windows and mechanical ventilation inlets. The laboratory room ventilation rate was not known.

Dragonite HP™ was first divided into ten aluminum trays covered with aluminum foil and dried at 120 °C overnight. Each tray contained *ca.* 100 g of dried HNTs. From the trays a total of 936 g HNT was poured from *ca.* 20 cm height into a 6.7 L stainless steel mixing bowl during 12 min. The bowl was attached to a mixer with a K-beater mixing tip (Titanium Major KMM020, Kenwood, 1 Kenwood Business Park, New Lane, Havant, UK). After pouring the HNTs, the mixing bowl was covered a splashguard and then 936 g of carvacrol was added through an inlet. The mixing power was increased gradually from 0 to 1 in power scale from 0 to 8 in arbitrary units. The mixing time was 18 min including a 3-minute pause when residual powder on the mixing bowl sides was scraped. After mixing, the resulting suspension was placed under vacuum at room temperature for 1 h induce carvacrol to loading into the HNT lumen. Finally, the mixture was packed and stored in amber glass containers.

3. Results and discussion

3.1. Dragonite HP™ powder characterization

Halloysite nanotubes (Dragonite HP™, Applied Minerals Inc., New York, US; CAS: 1332-58-7) is a natural aluminosilicate clay ($Al_2Si_2O_5(OH)_4{\cdot}nH_2O$; molecular weight 258.16 amu in anhydrous form) which mainly presents a hollow tubular morphology. According to the manufacturer, the inner diameter of the tube ranges from 15 to 45 nm and outer diameter from 50 to 70 nm. Length wise, 80 to 98% of the particles are $< 2\,\mu m$.

Supporting Information contains details of our Dragonite HP™ powder characterization (Figs. S1–S4 and Tables S1–S4). The bulk density measured by Mercury porosimetry was $0.73\,g\,cm^{-3}$ and apparent density was $2.11\,g\,cm^{-3}$ (Fig. S2 and Table S1, Supporting Information) and average surface area was $42 \pm 4\,m^2\,g^{-1}$ as determined by BET analysis nitrogen adsorption isotherms (Table S2, Supporting Information). The HNTs powder X-ray diffraction revealed that the major crystalline phases are kaolinite and halloysite 7A; whereas quartz is present as a minor phase (N/A wt%; Fig. S3, Supporting Information). The elemental composition as determined by inductively coupled plasma atomic emission spectroscopy, X-ray photoelectron spectroscopy, and Fourier-transform infrared spectroscopy are shown in Tables S3, S4, and Fig. S4, Supporting Information.

3.2. Airborne particle measurements

Particle concentration levels were measured in parallel with DiSCminis and respirable particles collectors from inside the fume hood, in the near field, the breathing zone, and at the incoming ventilation air supply (Fig. 1). At all measurement locations, the initial (at time point 10:10 in Fig. 2) particle number, N (cm^{-3}), and lung deposited surface area, *LDSA* ($\mu m^2\,cm^{-3}$), concentrations were measured to be *ca.* $14{,}000\,cm^{-3}$ and $38\,\mu m^2\,cm^{-3}$, respectively. After 90 min, N and *LDSA* values decreased to *ca.* $3000\,cm^{-3}$ and $14\,\mu m^2\,cm^{-3}$, respectively (see Fig. 2). In contrast, the mean particle diameter measured by the DiSCmini, $D_{p,DM}$ (nm), was initial 30 nm and increased within 90 min to ~53 nm, see Fig. 2c. Pouring was performed between 10:36–10:48 and at 10:55 the mixing process started and lasted for 28 min (Fig. 2). Two background concentrations were calculated for both the pouring (BG1) and the mixing (BG2) processes, *i.e.*, average concentrations measured before and after the process (Fig. 2c).

The pouring process increased the particle number concentrations in the fume hood from *ca.* $4800\,cm^{-3}$ up to $7700\,cm^{-3}$ for *ca.* 10 s (Fig. 2a). On average, the pouring process did not have a significant effect on the N concentrations within the fume hood (Fig. 2a; Table S5, Supporting Information). However, the *LDSA* peak concentrations increased from the BG1 level of 20.9 (± 1.5) $\mu m^2\,cm^{-3}$ to an average value of 27.3 (± 5.1) $\mu m^2\,cm^{-3}$ (Fig. 2b), and $D_{p,DM}$ increased from the BG1 diameter of 62 (± 4) nm to an average of 102 (± 18) nm (Fig. 2c). These peak concentrations were not observed outside the fume hood at far-field or the breathing zone (Fig. 2). The mixing step was not found to significantly increase the concentrations in the fume hood. There was no significant difference between the process concentrations and their respective background concentrations when averaged over the whole process period (see Table S5, Supporting Information).

The average respirable mass concentrations in the fume hood was $143\,\mu g\,m^{-3}$. Whereas, the average concentration values were below the detection limits in the near-field ($103\,\mu g\,m^{-3}$), breathing zone ($71\,\mu g\,m^{-3}$), and incoming ventilation air ($41\,\mu g\,m^{-3}$), respectively. The respirable mass sampling periods are shown in Fig. 2a.

3.3. Fiber measurements and analysis

A sample was collected for a scanning transmission electron microscopy (STEM) analysis during pouring of the Dragonite HP™ using a three stage micro inertial impactor. The sampling time was set to approximately 1 min and sample volume 0.5 L. STEM images were acquired for quantitative size analysis following a straight line going

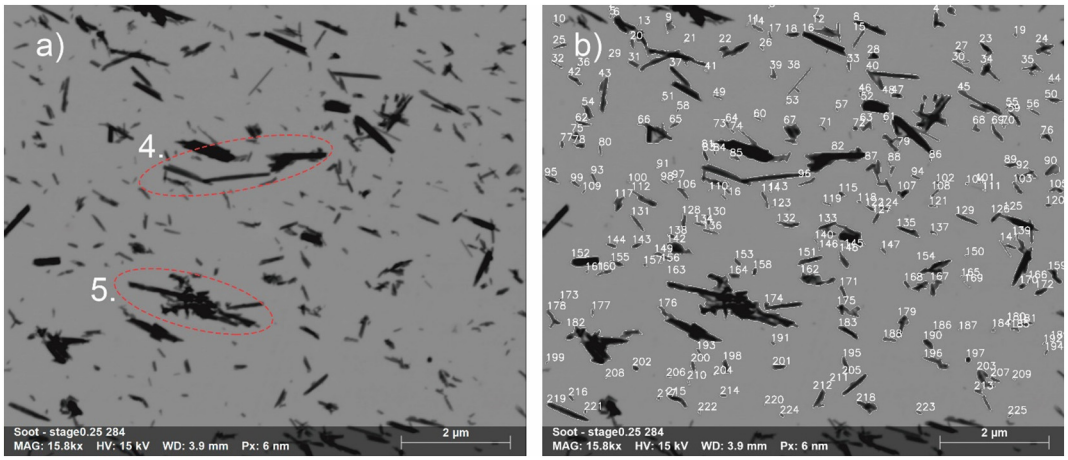

Fig. 3. Micrograph from the 3rd impactor stage (d_{50} = 50 nm) sampled during pouring of Dragonite HP™ a) before segmentation and b) after segmentation. Circled particles in a) fulfilled the aspect ratio > 3 and length > 2 µm and were labelled as 4 and 5 (see Fig. 4b).

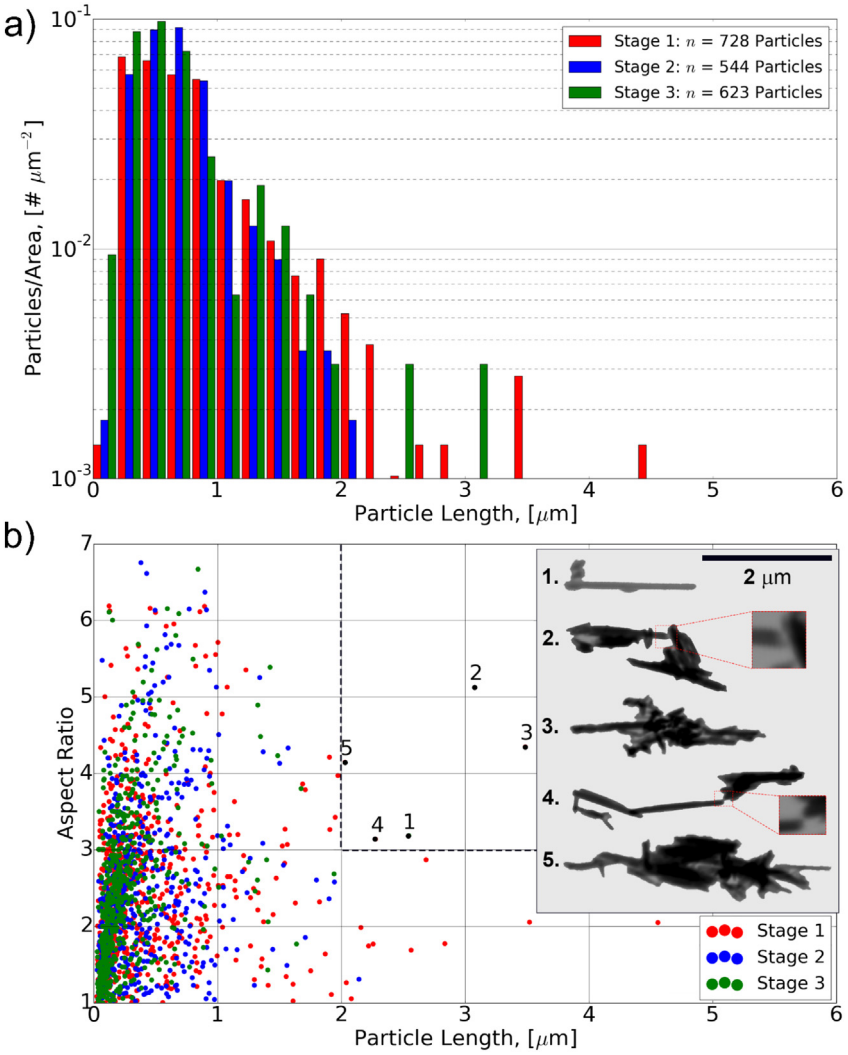

Fig. 4. Statistical analysis of the Micro Inertial Impactor samples: a) particle length distribution (raw counts μm^{-2}) and b) particles classified according to their aspect ratio where dashed line shows the region of particles with aspect ratio $>$ 3 and length $>$ 2 μm which are shown in the legend. In figure b) legend red squares shows 3× magnification from the particles intersection.

through the center of the impaction spot for each impactor stage, to capture any potential size distributions in the impaction patterns. Fig. 3 shows an example of images acquired from the last stage of the impactor both before and after segmentation. The particles were sized into 200 nm wide bins from 0 to 5000 nm according to bounding box longest dimension, $D_{BB,L}$, to illustrate their fibrous nature (Fig. 4a). Distribution of the deposited particles in different stages were similar and all detected particles were $<$ 5 μm long (Fig. 4). Note that the number of particles does not represent the total particle number count in the air sample volume.

A total of 1895 particles were analyzed from twenty images and classified according to their aspect ratio and length (Fig. 4b). Five individual fibers, with an aspect ratio $>$ 3 and length value $>$ 2 μm, were identified and numbered 1 to 5 (Fig. 4b). Particle no. 1 was a single HNT fiber with few small HNT fragments, and particles no. 2 to 5 consisted of multiple HNTs fibers (Fig. 4b). Particles no. 2 and 4 were fiber aggregates most likely formed by co-deposition (see Fig. 4b magnifications in the legend). Consequently, none of the analyzed particles fulfilled the paradigm of a WHO fiber.

In this study, the images were analyzed at a magnification level of 15,000 which corresponds to a pixel size of 6 nm. The image resolution was 1600 × 1381 which result to a graticule field, A_{gf} (m^2), of 8.0×10^{-11} m^2 and the number of graticule fields, n_{gf} (−), was 20. The particles were collected on three TEM grids where the single grid area was 7×10^{-6} m^2 and the total effective collection area, A_c (m^2), was 21×10^{-6} m^2. We found one fiber with a characteristic length above 2 μm. Assuming uniformly deposited particles across the collection grids the concentration of fibers $>$ 2 μm in length would be 27 fibers cm^{-3} according to the Eq. (1) in the Experimental section. According to the National Institute for Occupational Safety and Health (NIOSH) inter-laboratory variability (Ashley and O'Connor, 2016; NIOSH, 1994a, 1994b) there is a 90% probability, due to inter-laboratory variability, that other laboratories measures 0.2 to 8 fibers (−83% to +660% of the mean count) when one laboratory has found 1 fiber using our analytical conditions. Considering this subjective inter-laboratory uncertainty, the true concentration of $>$ 2 μm fibers could in our study be in the range from 4.5 to 200 fibers cm^{-3}. However, because the collection efficiency and distribution of deposited particles in the sampler applied here are not well known, the uncertainty range is higher.

Currently, there are no standard nanofiber collection techniques designed for workplace atmospheres. However, even using a perfect sampler, the challenging factors to detect a fiber with a thickness below 100 nm are:

- Low fiber density (m^{-2}) on the sample grid potentially as a fraction

of abundant other shorter fibers (see Fig. 4a)
- Presence of high background ultrafine particle concentrations in workplace atmospheres (Viitanen et al., 2017) that becomes visible in nanofiber detection.
- A small graticule field area due to a small pixel size and image resolution.

For an ideal single TEM grid sampler, with a 100% sampling efficiency and uniform particle deposition, the fiber density would be 7.1×10^7 fibers m^{-2} (71 fibers mm^{-2}) for a 0.5 L sample for a target fiber concentration of 1 fibers cm^{-3}. According to Eq. (2), only one fiber is expected to be found from *ca.* 180 images, when using the same graticule field as used in this study. According to NIOSH recommendation, at least 5.5 fibers should be counted to reduce the inter-laboratory upper limit variability to 300% (4 times) than the measured value. Thus, finding 5.5 fibers would increase the number of images to *ca.* 1000. Now, there should be a 90% probability that any laboratory would find a mean fiber count of 5.5 (range 2 to 22 fibers corresponding to an observed fiber concentration of 0.4 to 4 fibers cm^{-3}). Ensuring that the fiber concentration is below 1 fibers cm^{-3}, the counting should be made for a target concentration level of 0.25 fibers cm^{-3}. This would result in 4 times lower fiber density and increase the required number of images to 4000. If target fiber concentration would be reduced from 1 fibers cm^{-3} to 0.01 fibers cm^{-3}, as proposed for > 5 μm HARN, the required number of images would be 4×10^5 following the same strategy. Even-though automated electron microscopy and imaging technologies are progressing quickly these years (*e.g.* Temmerman et al., 2014), a different analytical strategy must be established to enforce proposed regulatory exposure limits on the level of 0.01 fibers cm^{-3}. A particular challenge is the fibers and rods with diameters in the few nm-range.

3.4. Risk assessment

Despite relatively extensive mining and industrial use of HNTs and the possibility that a fraction of the HNTs may fulfil the fiber paradigm, we were not able to find occupational exposure studies considering occupational exposure to HNTs (Debia et al., 2016; Ding et al., 2017). In this study, we showed that pouring of *ca.* 100 g HNTs at rate of 0.5 kg min^{-1} releases high amounts of particles (release rate N/A) leading to airborne particle concentrations of up to 2900 particles cm^{-3} for *ca.* 10 s (Fig. 2a). The DiSCmini particle number concentration measurement is sensitive to impaction of large particles at the diffusion stage so the reliability of this measurement is challenging to estimate (Koivisto et al., 2016).

In the fume hood the LDSA concentrations were on average elevated 0.7 $\mu m^2 cm^{-3}$ from the BG1 level of 20.9 $\mu m^2 cm^{-3}$ (see Table S5, Supporting Information). During 8-h exposure this corresponds to a human equivalent dose of 1×10^{-4} $cm^2 g^{-1}$ which is *ca.* 10^3 times less than $NOEL_{1/100}$ of 0.11 $cm^2 g^{-1}$ for GBPs assigned by Koivisto et al. (2016). The background LDSA concentration is also *ca.* half of the average geometric mean urban background levels of 44.2 $\mu m^2 cm^{-3}$ (geometric standard deviation 2.2) in European cities (Koivisto et al., 2016). Moreover, the chemical composition of the HNTs analogous bulk material is kaolinite for which the OEL varies between 2 (respirable fraction) and 10 (total dust) mg m^{-3} in Europe. In our measurements, we found (within the fume hood) a respirable mass concentration of background particles and HNTs fibers of 143 μg m^{-3}, which is well below the lowest OEL in Europe. These analyses represent the potential exposure if HNTs had been handled without using the fume hood when the potential for exposure is the highest. The concentrations outside the fume hood, at near-field and breathing zone, remained at the background concentration level during pouring.

We did not find any > 5 μm fibers after analyzing 1895 particles. The longest confirmed single fiber was *ca.* 2 μm in length (Fig. 4b). However, due to the small analyzed sample, the concentration levels of fibers between 2 and 5 μm and > 5 μm in length can be estimated only with a very large uncertainty interval. Twenty images were analyzed while 4×10^4 images should have been assessed before any conclusions can be made in the OEL range of 0.1 to 2 fibers cm^{-3} and 4×10^5 times more for the proposed OEL for > 5 μm HARN (Schulte et al., 2010; Boulanger et al., 2014; Mihalache et al., 2017). We could not detect any fibers or fiber-related risks outside the fume hood according to the DiSCmini and respirable mass concentration measurements. This is in line with Fonseca et al. (2018) who showed that a fume hood is an efficient exposure control for nanomaterial powder handling.

On the other hand, there is limited data regarding the pulmonary toxicity of HNTs exposure. Sub-chronic inhalation studies in rats using CNTs which were too short to fulfil the fiber paradigm resulted in sustained inflammation and fibrosis (Pauluhn, 2010; Boulanger et al., 2014; Ma-Hock et al., 2009) with a lowest-observed-adverse-effect-level of 100 μg m^{-3}. NIOSH (2013) and researchers from the European Joint Research Centre have both proposed OELs for carbon nanotubes in the order of 1 μg m^{-3} (Mihalache et al., 2017). If HNTs have similar effects following pulmonary exposure as CNTs with similar dimensions, then the observed exposure levels of 143 μg m^{-3}, including background particles and HNTs from the pouring process, would be considered high as it exceeds the proposed OEL for CNTs (of any length) by > 100 fold. Currently, the HNTs inhalation exposure risk assessment requires more pulmonary toxicity studies, preferably conducted with direct inhalation exposure.

4. Conclusions

The longest individual HNTs fiber observed was 2 μm long and there were no fibers with lengths > 5 μm. By following the NIOSH guidance, the uncertainties related to fiber count were too high to estimate fiber concentration levels. To reach occupational exposure limits in the range of 1 cm^{-3}, the analysis should have been done at least for 4000 images, which was not reasonably feasible due to limited resources and uncertainties on the collection efficiency of the applied sampling technique. An improved sampling and analytical strategy is required to quantify the potential presence of nanofibers at the currently proposed 0.01 cm^{-3} for high aspect ratio nanomaterial fibers in the working environment. The challenge is particularly great for fibers with diameters in the few nm-range. More sophisticated particle sampling and comprehensive image analysis techniques are needed before regulatory exposure limits in units of fibers cm^{-3} are implemented to cover fibers < 100 nm in diameter. The risk assessment based on surface area and mass concentrations did not show significant exposure risk when compared to $NOEL_{1/100}$ level for granular biodurable particles or OEL level of the analogous bulk material in chemical composition, kaolinite, respectively.

Conflict of interest

There are no conflicts of interest to declare.

Acknowledgements

This project has received funding from the European Union's Horizon 2020 research and innovation programme under grant agreement No 720815. Any dissemination of results must indicate that it reflects only the author's view and that the Commission is not responsible for any use that may be made of the information it contains.

Appendix A. Supplementary data

Characterization of Dragonite™ powder, average concentrations, and instrument comparison. Supplementary data associated with this article can be found, in the online version, at https://doi.org/10.1016/j.impact.2018.04.003.

References

Ahmed, F.R., Shoaib, M.H., Azhar, M., Um, S.H., Yousuf, R.I., Hashmi, S., et al., 2015. In-vitro assessment of cytotoxicity of halloysite nanotubes against HepG2, HCT116 and human peripheral blood lymphocytes. Colloids Surf. B Biointerfaces 135, 50–55.

Ashley, K., O'Connor, P.F., 2016. NIOSH Manual of Analytical Methods (NMAM), 5th Ed. . Available online: www.cdc.gov/niosh/nmam [Accessed 27st February 2018].

Bau, S., Payet, R., Witschger, O., Jankowska, E., 2017. Performance study of portable devices for the real-time measurement of airborne particle number concentration and size (distribution). J. Phys. Conf. 838, p.012001.

Bonifacio, B.A., Gentile, P., Ferreira, A.M., Cometa, S., De Giglio, E., 2017. Insight into halloysite nanotubes-loaded gellan gum hydrogels forsoft tissue engineering applications. Carbohydr. Polym. 163, 280–291.

Boulanger, G., Andujar, P., Pairon, J.C., Billon-Galland, M.A., Dion, C., Dumortier, P., et al., 2014. Quantification of short and long asbestos fibers to assess asbestos exposure: a review of fiber size toxicity. Environ. Health 21 (13), 59.

Bradski, G., 2000. The OpenCV Library.

De Volder, M.F., Tawfick, S.H., Baughman, R.H., Hart, A.J., 2013. Carbon nanotubes: present and future commercial applications. Science 339, 535–539.

Debia, M., Bakhiyi, B., Ostiguy, C., Verbeek, J.H., Brouwer, D.H., Murashov, V., 2016. A systematic review of reported exposure to engineered nanomaterials. Ann. Occup. Hyg. 60, 916–935.

Ding, Y., Kuhlbusch, T.A., Van Tongeren, M., Jiménez, A.S., Tuinman, I., Chen, R., et al., 2017. Airborne engineered nanomaterials in the workplace-a review of release and worker exposure during nanomaterial production and handling processes. Hazard. Mater. 322, 17–28.

ECHA, 2016. Guidance on Information Requirements and Chemical Safety Assessment, Chapter R.15: Consumer Exposure Assessment. Available at. https://echa.europa.eu/documents/10162/13632/information_requirements_r15_en.pdf, Accessed date: 27 February 2018.

Fonseca, A.S., Kuijpers, E., Kling, K.I., Levin, M., Koivisto, A.J., Nielsen, S.H., et al., 2018. Particle release and control of worker exposure during laboratory-scale synthesis, handling and simulated spills of manufactured nanomaterials in fume-hoods. J. Nanopart. Res. 20, 48.

Gao, N., Keane, M.J., Ong, T., Wallace, W.E., 2000. Effects of simulated pulmonary surfactant on the cytotoxicity and DNA-damaging activity of respirable quartz and kaolin. J. Toxicol. Environ. Health A 60, 153–167.

Gebel, T., Foth, H., Damm, G., Freyberger, A., Kramer, P.J., Lilienblum, W., et al., 2014. Manufactured nanomaterials: categorization and approaches to hazard assessment. Arch. Toxicol. 88, 2191–2211.

Gutiérrez, E., Bono, F., 2013. Review of Industrial Manufacturing Capacity for Fibre-reinforced Polymers as Prospective Structural Components in Shipping Containers. JRC Scientific and Policy Reports, JRC77823.

Hanif, M., Jabbar, F., Sharif, S., Abbas, G., Farooq, A., Aziz, M., 2016. Halloysite nanotubes as a new drug-delivery system: a review. Clay Miner. 51, 469–477.

Harrison, P., Holmes, P., Bevan, R., Kamps, K., Levy, L., Greim, H., 2015. Regulatory risk assessment approaches for synthetic mineral fibres. Regul. Toxicol. Pharmacol. 73, 425–441.

Huang, J., Tang, Z.H., Zhang, X.H., Guo, B.C., 2016. Halloysite polymer nanocomposites. In: Nanosized Tubular Clay Minerals Halloysite and Imogolite, 1st ed. Elsevier, pp. 509–533.

Hwang, J., Ramachandran, G., Raynor, P.C., Alexander, B.H., Mandel, J.H., 2014. The relationship between various exposure metrics for elongate mineral particles (EMP) in the taconite mining and processing industry. J. Occup. Environ. Hyg. 11, 613–624.

Jin, J., Ouyang, J., Yang, H., 2017. Pd nanoparticles and MOFs synergistically hybridized halloysite nanotubes for hydrogen storage. Nanoscale Res. Lett. 12, 240.

Jaurand, M.-C., 2017. An overview on the safety of tubular clay minerals. Elsevier 485–508.

Jensen, A.C.Ø., Levin, M., Koivisto, A.J., Kling, K.I., Saber, A.T., Koponen, I.K., 2015. Exposure assessment of particulate matter from abrasive treatment of carbon and glass fibre-reinforced epoxy-composites - two case studies. Aerosol Air Qual. Res. 15, 1906–1916.

Joussein, E., Petit, S., Churchman, J., Theng, B., Righi, D., Delvaux, B., 2005. Halloysite clay minerals - a review. Clay Miner. 40, 383–426.

Kandler, K., Benker, N., Bundke, U., Cuevas, E., Ebert, M., Knippertz, P., et al., 2007. Chemical composition and complex refractive index of Saharan Mineral Dust at Izaña, Tenerife (Spain) derived by electron microscopy. Atmos. Environ. 41, 8058–8074.

Kandler, K., Lieke, K., Benker, N., Emmel, C., Küpper, M., Müller-Ebert, D., et al., 2011. Electron microscopy of particles collected at Praia, Cape Verde, during the Saharan Mineral Dust Experiment: particle chemistry, shape, mixing state and complex refractive index. Tellus B 63, 475–496.

Kling, K.I., Levin, M., Jensen, A.C.Ø.K., Jensen, A., Koponen, I.K., 2016. Size-resolved characterization of particles and fibers released during abrasion of fiber-reinforced composite in a workplace influenced by ambient background sources. Aerosol Air Qual. Res. 16, 11–24.

Koivisto, A.J., Kling, K.I., Levin, M., Fransman, W., Gosens, I., Cassee, F.R., et al., 2016. First order risk assessment for nanoparticle inhalation exposure during injection molding of polypropylene composites and production of tungsten-carbide-cobalt fine powder based upon pulmonary inflammation and surface area dose. NanoImpact 6, 30–38.

Koivisto, A.J., Kling, K.I., Fonseca, A.S., Bluhme1, A.B., Moreman, M., Yu, M., et al., 2018. Dip coating of air purifier ceramic honeycombs with photocatalytic TiO_2 nanoparticles: a case study for occupational exposure. Sci. Total Environ. 630, 1283–1291.

Krepker, M., Shemesh, R., Poleg, D.Y., Kashi, Y., Vaxman, A., Segal, E., 2017. Active food packaging films with synergistic antimicrobial activity. Food Control 76, 117–126.

Lai, X., Agarwal, M., Lvov, Y.M., Pachpande, C., Varahramyan, K., Witzmann, F.A., 2013. Proteomic profiling of halloysite clay nanotube exposure in intestinal cell co-culture. J. Appl. Toxicol. 33, 1316–1329.

Lieke, K., Kandler, K., Scheuvens, D., Emmel, C., Von Glahn, C., Petzold, A., et al., 2011. Particle chemical properties in the vertical column based on aircraft observations in the vicinity of Cape Verde Islands. Tellus B 63, 497–511.

Lieke, K.I., Rosenørn, T., Pedersen, J., Larsson, D., Kling, J., Fuglsang, K., et al., 2013. Micro- and nanostructural characteristics of particles before and after an exhaust gas recirculation system scrubber. Aerosol Sci. Technol. 47, 1038–1046.

Lippmann, M., 1988. Asbestos exposure indices. Environ. Res. 46, 86–106.

Lippmann, M., 2014. Toxicological and epidemiological studies on effects of airborne fibers: coherence and public health implications. Crit. Rev. Toxicol. 44, 643–695.

Liu, M., Jia, Z., Jia, D., Zhou, C., 2014. Recent advance in research on halloysite nanotubes-polymer nanocomposite. Prog. Polym. Sci. 39, 1498–1525.

Liu, M., He, R., Yang, J., Long, Z., Huang, B., Liu, Y., et al., 2016. Polysaccharide-halloysite nanotube composites for biomedical applications: a review. Clay Miner. 51, 457–467.

Lvov, Y.M., Shchukin, D.G., Mohwald, H., Price, R.R., 2008. Halloysite clay nanotubes for controlled release of protective agents. ACS Nano 2, 814–820.

Lvov, Y.M., DeVilliers, M.M., Fakhrullin, R.F., 2016a. The application of halloysite tubule nanoclay in drug delivery. Adv. Mater. 28, 1227–1250.

Lvov, Y.M., Wang, W., Zhang, L., Fakhrullin, R., 2016b. Halloysite clay nanotubes for loading and sustained release of functional compounds. Adv. Mater. 28, 1227–1250.

Ma-Hock, L., Treumann, S., Strauss, V., Brill, S., Luizi, F., Mertler, M., et al., 2009. Landsiedel. Inhalation toxicity of multiwall carbon nanotubes in rats exposed for 3 months. Toxicol. Sci. 2009 (112), 468–481.

Makaremi, M., Pasbakhsh, P., Cavallaro, G., Lazzara, G., Aw, Y.K., Lee, S.M., et al., 2017. Effect of morphology and size of halloysite nanotubes on functional pectin bionanocomposites for food packaging applications. ACS Appl. Mater. Interfaces 9, 17476–17488.

Mihalache, R., Verbeek, J., Graczyk, H., Murashov, V., van Broekhuizen, P., 2017. Occupational exposure limits for manufactured nanomaterials, a systematic review. Nanotoxicology 11, 7–19.

Molina, D.K., DiMaio, V.J., 2012. Normal organ weights in men: part II-the brain, lungs, liver, spleen, and kidneys. Am. J. Forensic Med. Pathol. 33, 68–372.

Moreno-Horn, M., Gebel, T., 2014. Granular biodurable nanomaterials: no convincing evidence for systemic toxicity. Crit. Rev. Toxicol. 44, 849–875.

Nan, A., Bai, X., Son, S.J., Lee, S.B., Ghandehari, H., 2008. Cellular uptake and cytotoxicity of silica nanotubes. Nano Lett. 8, 2150–2154.

Nguyen, Q.T., Kjær, K.H., Kling, K.I., Boesen, T., Bilde, M., 2017. Impact of fatty acid coating on the CCN activity of sea salt particles. Tellus B 69 (1).

NIOSH, 1994a. Method for determination of asbestos in air using positive phase contrast microscopy. In: NIOSH Method 7400. National Institute for Occupational Safety and Health First Issued: 1985, Cincinnati, OH (Current revision).

NIOSH, 1994b. Method for determination of asbestos in air using transmission electron microscopy. In: NIOSH Method 7402. National Institute for Occupational Safety and Health 1986, Cincinnati, OH (Current revision).

NIOSH, 2013. Occupational Exposure to Carbon Nanotubes and Nanofibers, Publication No. 2013–145. Available at. https://www.cdc.gov/niosh/docs/2013-145/pdfs/2013-145.pdf, Accessed date: 27 February 2018.

Nielsen, G.D., Koponen, I.K., 2018. Insulation fiber deposition in the airways of men and rats. A review of experimental and computational studies. Regul. Toxicol. Pharmacol. 94, 252–270.

Pauluhn, J., 2010. Subchronic 13-week inhalation exposure of rats to multiwalled carbon nanotubes: toxic effects are determined by density of agglomerate structures, not fibrillar structures. Toxicol. Sci. 113, 226–242.

Poulsen, S.S., Saber, A.T., Williams, A., Andersen, O., Købler, C., Atluri, R., et al., 2015. MWCNTs of different physicochemical properties cause similar inflammatory responses, but differences in transcriptional and histological markers of fibrosis in mouse lungs. Toxicol. Appl. Pharmacol. 284, 16–32.

Poulsen, S.S., Jackson, P., Kling, K., Knudsen, K.B., Skaug, V., Kyjovska, Z.O., et al., 2016. Multi-walled carbon nanotube physicochemical properties predict pulmonary inflammation and genotoxicity. Nanotoxicology 10, 1263–1275.

Poulsen, S.S., Knudsen, K.B., Jackson, P., Weydahl, I.E., Saber, A.T., Wallin, H., et al., 2017. Multi-walled carbon nanotube-physicochemical properties predict the systemic acute phase response following pulmonary exposure in mice. PLoS One 12, e0174167.

Saber, A.T., Lamson, J.S., Jacobsen, N.R., Ravn-Haren, G., Hougaard, K.S., Nyendi, A.N., et al., 2013. Particle-induced pulmonary acute phase response correlates with neutrophil influx linking inhaled particles and cardiovascular risk. PLoS One e69020, 20138.

Saber, A.T., Jacobsen, N.R., Jackson, P., Poulsen, S.S., Kyjovska, Z.O., Halappanavar, S., et al., 2014. Particle-induced pulmonary acute phase response may be the causal link between particle inhalation and cardiovascular disease. Wiley Interdiscip. Rev. Nanomed. Wiley Interdiscip. Rev. Nanomed. Nanobiotechnol. 6, 517–531.

Sahiner, N., Sengel, S.B., 2017. Environmentally benign halloysite clay nanotubes as alternative catalyst to metal nanoparticles in H2 production from methanolysis of sodium borohydride. Fuel Process. Technol. 158, 1–8.

Saif, M.J., Asif, H.M., 2015. Escalating applications of halloysite nanotubes. J. Chil. Chem. Soc. 60, 2949–2953.

Schmid, O., Stoeger, T., 2016. Surface area is the biologicallymost effective dosemetric for acute nanoparticle toxicity in the lung. J. Aerosol Sci. 99, 133–143.

Schulte, P.A., Murashov, V., Zumwalde, R., Kuempel, E.D., Geraci, C.L., 2010. Occupational exposure limits for nanomaterials: state of the art. Nanopart. Res. 12, 1971–1987.

Shemesh, E., Krepker, M., Nitzan, N., Vaxman, A., Segal, E., 2016. Active packaging containing encapsulated carvacrol for control of postharvest decay. Rotem. Shemesh. Postharvest Biol. Technol. 118, 175–182.
Stacey, P., Lee, T., Thorpe, A., Roberts, P., Frost, G., Harper, M., 2014. Collection efficiencies of high flow rate personal respirable samplers when measuring Arizona road dust and analysis of quartz by X-ray diffraction. Ann. Occup. Hyg. 58, 512–523.
Stanton, M.F., Layard, M., Tegeris, A., Miller, E., May, M., Morgan, E., et al., 1981. Relation of particle dimension to carcinogenicity in amphibole asbestoses and other fibrous minerals. J. Natl. Cancer Inst. 67, 965–975.
Stayner, L., Kuempel, E., Gilbert, S., Hein, M., Dement, J., 2008. An epidemiological study of the role of chrysotile asbestos fibre dimensions in determining respiratory disease risk in exposed workers. Occup. Environ. Med. 65, 613–619.
Stayner, L., Welch, L.S., Lemen, R., 2013. The worldwide pandemic of asbestos-related diseases. Annu. Rev. Public Health 34, 205–216.
Tas, C.E., Hendessi, S., Baysal, M., Unal, S., Cebeci, F.C., Menceloglu, Y.Z., et al., 2017. Halloysite nanotubes/polyethylene nanocomposites for active food packaging materials with ethylene scavenging and gas barrier properties. Food Bioprocess Tech. 10, 789–798.
Temmerman, P.-J.D., Verleysen, E., Lammertyn, J., Mast, J., 2014. Semi-automatic size measurement of primary particles in aggregated nanomaterials by transmission electron microscopy. Powder Technol. 2014 (261), 191–200.
Vergaro, V., Abdullayev, E., Lvov, Y.M., Zeitoun, A., Cingolani, R., Rinaldi, R., et al., 2010. Cytocompatibility and uptake of halloysite clay nanotubes. Biomacromolecules 11, 820–826.
Viitanen, A.-K., Uuksulainen, S., Koivisto, A.J., Hämeri, K., Kauppinen, T., 2017. Workplace measurements of ultrafine particles - a literature review. Ann. Work Expo. Health 61, 749–758.
Wei, H., Wang, Y., Guo, J., Shen, N.Z., Jiang, D., Zhang, X., et al., 2015. Advanced micro/nanocapsules for self-healing smart anticorrosion coatings. J. Mater. Chem. A 3, 469–480.
Yang, H., Zhang, Y., Ouyang, J., 2016. Physicochemical properties of halloysite. In: Nanosized Tubular Clay Minerals Halloysite and Imogolite, 1st ed. Elsevier, pp. 67–91.
Yendluri, R., Otto, D.P., De Villiers, M.M., Vinokurov, V., Lvov, Y.M., 2017. Application of halloysite clay nanotubes as a pharmaceutical excipient. Int. J. Pharm. 521, 267–273.
Yu, L., Wang, H., Zhang, Y., Zhang, B., Liu, J., 2016. Recent advances in halloysite nanotube derived composites for water treatment. Environ. Sci.: Nano 28–44.